Available online at www.sciencedirect.com
SCIENCE DIRECT®
Journal of Power Sources 139 (2005) 325–341
JOURNAL OF POWER SOURCES
www.elsevier.com/locate/jpowsour

Hydrothermal MnO_2: synthesis, structure, morphology and discharge performance

Daud K. Walanda, Geoffrey A. Lawrance, Scott W. Donne*

Discipline of Chemistry, School of Environmental and Life Sciences, University of Newcastle, Callaghan, NSW 2308, Australia

Received 29 April 2004; received in revised form 30 June 2004; accepted 30 June 2004
Available online 8 September 2004

Abstract

Digestion of Mn_2O_3 in a range of H_2SO_4 solutions (0.01–0 M), at a variety of temperatures (20–140 °C) has led to the formation of a series of kinetically stable manganese dioxide samples via a dissolution-precipitation mechanism that involves disproportionation of a soluble Mn(III) intermediate. The resultant manganese dioxide samples are characterized in terms of their domain of phase stability, chemical composition, structure, morphology and electrochemical performance. γ-MnO_2 predominates at all but high H_2SO_4 concentrations (>5 M), where α-MnO_2 is formed, and high temperatures (>80 °C) where β-MnO_2 is formed. The structural variety of γ-MnO_2 in this domain of stability is interpreted in terms of: (i) the fraction of De Wolff defects (P_r), which is found to increase as the H_2SO_4 concentration is decreased and the temperature is increased; (ii) microtwinning (T_w), which despite being less statistically significant, is found to follow a similar trend; (iii) the cation vacancy fraction; (iv) the Mn(III) fraction. Both the latter structural properties decrease as the temperature is increased; but decreasing the H_2SO_4 concentration leads to a decrease in cation vacancy fraction and an increase in Mn(III) fraction. These structural characteristics, in particular the De Wolff defects, are interpreted on a molecular level in terms of soluble Mn(III) intermediate condensation, in which the electrolyte conditions determine the relative proportions of equatorial-axial edge sharing (ramsdellite domains only), and equatorial-axial corner sharing (both ramsdellite and pyrolusite domains) that occurs. Morphological differentiation is easily established due to the different characteristics of each phase. γ-MnO_2 exists as fine needles (250 nm × 50 nm), β-MnO_2 is formed as much larger columns (1 μm × 100 nm), while α-MnO_2 is present as small spheres of up to 400 nm in diameter. Electrochemical characterization by voltammetry in an aqueous 9 M KOH electrolyte demonstrates that the performance of γ-MnO_2 samples is comparable with that of commercial EMD, whereas α- and β-MnO_2 suffer from diffusional limitations which lower their operating voltage. For γ-MnO_2, superior performance results when lower temperatures and H_2SO_4 concentrations are used. This corresponds to intermediate levels of De Wolff defects and microtwinning, and to a cation vacancy fraction minimum.

Keywords: Manganese dioxide; Hydrothermal synthesis; Phase diagram; Electrochemical performance

1. Introduction

Manganese dioxide is by far the most common electroactive cathode material used in primary batteries. This is because it possesses a unique combination of beneficial physicochemical, electrochemical and economic properties. In particular, manganese dioxide with suitably high density and purity, as well as adequate electrochemical activity under a range of discharge conditions, can be produced efficiently and relatively inexpensively on a commercial scale.

Commercial synthesis involves electrodeposition of manganese dioxide (EMD) on to a titanium anode from a hot aqueous solution of H_2SO_4 and $MnSO_4$ [1]. The relevant synthesis variables have large ranges, i.e., anodic current densities in the range 10–100 A m^{-2}, temperatures in the range 85–99 °C, H_2SO_4 concentrations from 0.05 to 0.5 M, and $MnSO_4$ concentrations from 0.1 to 2.0 M. While almost any combination of these variables will lead to the deposition of γ-MnO_2 (the preferred structure for electrochemical applications), the

* Corresponding author. Fax: +61 279 215472.
E-mail address: scott.donne@newcastle.edu.au (S.W. Donne).

0378-7753/$ – see front matter © 2004 Elsevier B.V. All rights reserved.
doi:10.1016/j.jpowsour.2004.06.062

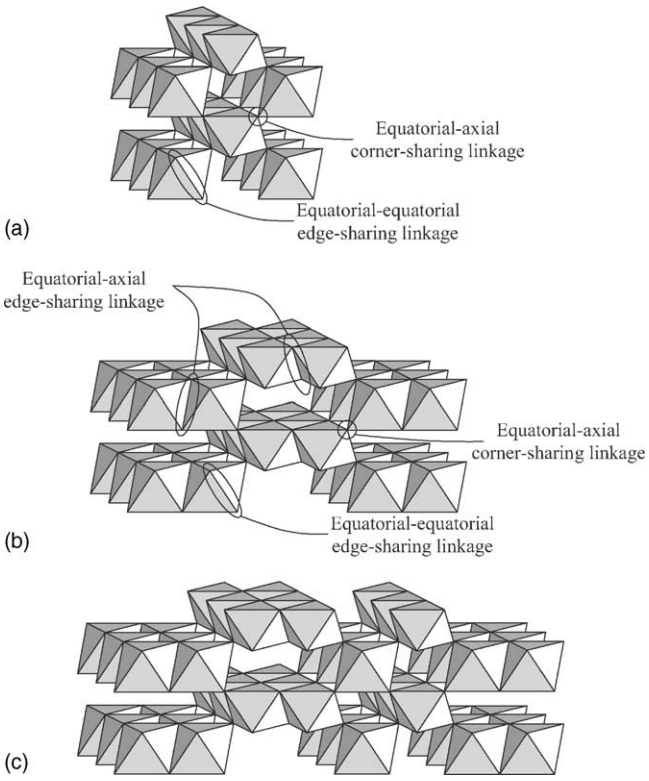

Fig. 1. Schematic structural diagrams of (a) pyrolusite (β-MnO_2); (b) ramsdellite; (c) De Wolff's model for γ-MnO_2 showing intergrowth between pyrolusite and ramsdellite domains.

variable ranges that produce a superior material are very narrow indeed [2].

The most effective basic description of the γ-MnO_2 structure was originally proposed by De Wolff [3] to consist of a micro-scale intergrowth of the ramsdellite and pyrolusite (β-MnO_2) forms of manganese dioxide [3]. The structure of these two basic forms can be described as a hexagonal close-packed array of oxide ions in which half of the available octahedral sites are selectively filled with Mn(IV) ions so as to form tunnels in the *c*-direction. For pyrolusite (β-MnO_2) and ramsdellite, these tunnels are (1 × 1) and (1 × 2) octahedral units in size, respectively. Schematic diagrams of pyrolusite, ramsdellite and De Wolff's model for γ-MnO_2 are shown in Fig. 1.

Since De Wolff's original model, others have made refinements. Ruetschi [4] introduced the cation vacancy model in an attempt to explain a number of physicochemical properties of γ-MnO_2. He suggested that within the hexagonal close-packed framework of oxide anions a fraction of Mn(IV) ions have been replaced by Mn(III) (*y*), and that a fraction of Mn(IV) ions are absent altogether (*x*). The positive charge deficiency is compensated by an appropriate number of protons located on adjacent oxide ions, i.e.

$$(Mn^{4+})_{1-x-y}(Mn^{3+})_y(\square)_x(O^{2-})_{2-4x-y}(OH^-)_{4x+y} \quad (1)$$

where □ represents a cation vacancy. Typical ranges for *x* and *y* are 0.06–0.08 and 0.04–0.12, respectively. It is these protons that constitute structural water within γ-MnO_2.

The most recent quantitative structural model for γ-MnO_2 [5] makes use of De Wolff's initial proposal, and includes the concepts of structural microtwinning in the 0 2 1 and 0 6 1 planes of ramsdellite. This model has been successful in that it has accounted for a number of previously unexplained features of the X-ray diffraction (XRD) pattern of γ-MnO_2. Although physical evidence to support the presence of microtwinning was apparent in some early high resolution TEM work [6], recent electron diffraction studies [7] have cast doubt on whether microtwinning does actually exist.

Considerable research has also been conducted on the electrochemical behaviour of γ-MnO_2 in concentrated alkaline electrolytes. This has focused on the discharge mechanism and the search for materials with superior electrochemical performance characteristics. The basis for the currently accepted discharge mechanism (Mn(IV) → Mn(III)) was proposed by Kozawa et al. [8–13], and is based on proton and electron insertion into the manganese dioxide structure (Fig. 2). The cathode in an alkaline Zn/MnO_2 cell essentially consists of an intimate mixture of electrolytic manganese dioxide (EMD) and a small proportion of graphite wetted with electrolyte. An electron from the external circuit passes through the graphite into the manganese dioxide structure where it reduces a Mn(IV) ion to Mn(III). For charge compensation (cf. Eq. (1)), a water molecule on the manganese dioxide surface dissociates into a proton, which is inserted into the structure, and an OH^- ion, which remains in the electrolyte. Additional capacity (other than that on the surface) can be extracted from the manganese dioxide by the inserted protons and electrons diffusing away from the surface into the bulk of the solid. The rate of this diffusion compared with

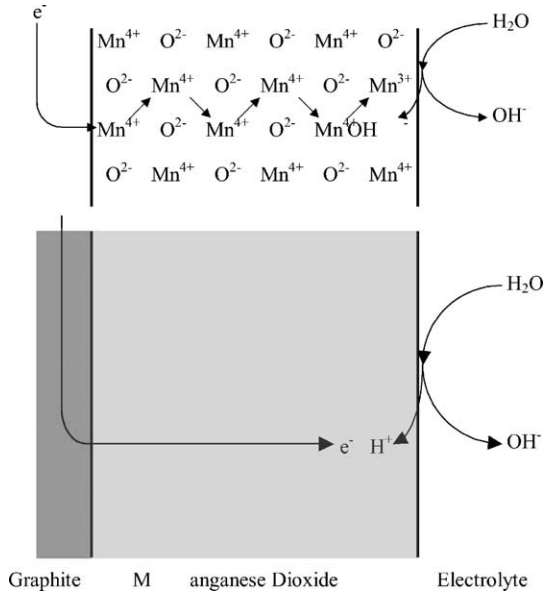

Fig. 2. Schematic diagram of electron–proton mechanism for reduction of γ-MnO_2 in concentrated alkaline electrolytes.

the rate of discharge determines the efficiency of manganese dioxide reduction.

A number of later research efforts [14–18] noticed the presence of distinct reduction processes during what is nominally the Mn(IV) → Mn(III) reduction step. These were variously ascribed to the reduction of different domains within the γ-MnO_2 structure, i.e., from highest to lowest voltage, Mn(IV) ions on the surface or near structural defects, in ramsdellite and then in pyrolusite domains. While this proposal seems logical, final confirmation is still necessary.

Although electrodeposition is employed commercially to produce γ-MnO_2, it is not the sole route to this material. In this work, we have used an acid digestion technique [19–22] to prepare a series of manganese dioxide samples with different structures and morphologies. This synthetic technique has been chosen (as opposed to electrodeposition) because of its simplicity and greater flexibility in producing different samples. Furthermore, as will be apparent, an assessment of sample morphology is straightforward in this case. Electrochemical characterization has been subsequently applied to complete the data set.

2. Experimental

2.1. Synthesis

Mn_2O_3 was used as a starting material. It was prepared by heating commercially available EMD (Delta EMD Australia Pty Limited) in a furnace at 550 °C for 24 h, after which time it was spectroscopically pure.

The general synthesis method involved digesting Mn_2O_3 in H_2SO_4 solutions of different concentration (0.01–10.0 M) at various temperatures (ambient–140 °C). For temperatures up to and including 80 °C, 10.00 g of Mn_2O_3 was suspended in 100 cm^3 of acid of a given concentration in a 250 cm^3, glass-stoppered, Erlenmeyer flask. For higher temperature experiments, 1.00 g of Mn_2O_3 was placed in a PTFE-lined, acid digestion bomb (PARR) together with 15 cm^3 of H_2SO_4 solution. Irrespective of the digestion vessel, the suspension was left at temperature for 1 week, with regular agitation to ensure suspension. After this time, the suspension was filtered and washed thoroughly with Milli-Q ultra-pure water. The resulting solids were then dried in air at 60 °C.

2.2. Chemical composition

2.2.1. n in MnO_n

The value of n in MnO_n for each sample was determined using the potentiometric titration approach of Vetter and Jaeger [23]. 0.100 g of manganese dioxide sample was dissolved in 25.0 cm^3 of acidified (10% H_2SO_4) 0.25 M $FeSO_4$ to reduce all Mn(III) and Mn(IV) species to soluble Mn(II). Formally, the manganese in MnO_n can be written as $(Mn^{IV}O_2)_{1-r}\cdot(Mn^{III}OOH)_r$ where r is related to n via

$$n = \frac{4-r}{2} \tag{2}$$

In terms of n, there are therefore $(2n-3)$ Mn(IV) ions and $(4-2n)$ Mn(III) ions, hence their reduction with Fe(II) can be written as

$$MnO_n + (2n-2)Fe^{2+} + (2n)H^+ \rightarrow Mn^{2+} + (2n-2)Fe^{3+} + nH_2O \tag{3}$$

Any Fe(II) remaining in solution after digestion can be potentiometrically back-titrated with standardized (oxalate method [24]) 0.02 M $KMnO_4$ (V_1) to provide an indication of the amount of Mn(III) and Mn(IV) species present.

Sufficient tetra sodium pyrophosphate ($Na_4P_2O_7\cdot10H_2O$) was added to the titration vessel until the solution pH was in the range 6–7. A second potentiometric titration was conducted using the same $KMnO_4$ solution, this time to determine the total manganese content of the sample (V_2). The value of n in MnO_n was then calculated using

$$n = 1 + \frac{5(V_0 - V_1)}{2(4V_2 - V_1)} \tag{4}$$

where V_0 is a replicate of the first titration in the absence of any sample.

2.2.2. Surface water and structural water

The surface water content of each manganese dioxide sample was determined by heating 0.500 g (m_0) of sample in air in an oven at 110 °C for 2 h. After cooling to ambient temperature in a dessicator the sample was re-weighed (m_1). The same sample was then heat-treated at 400 °C in air for another 2 h. After cooling in a dessicator, the sample was again re-weighed (m_2). The surface and structural water contents are given by

$$\text{surface water}(\%H_2O_{Su}) = \frac{m_0 - m_1}{m_0} \times 100\% \tag{5a}$$

$$\text{structural water}(\%H_2O_{St}) = \frac{m_1 - m_2}{m_1} \times 100\% \tag{5b}$$

Expressing the structural water content in this way (dry basis) avoids any variability being introduced from the ambient laboratory conditions that would affect the surface water content.

2.2.3. Total manganese content, and Mn(IV) and Mn(III) fractions

Quantification of the distributions of manganese species in each sample requires the use of a standardized $KMnO_4$ solution, as well as expression of the results on a dry basis. The total manganese content ($\%Mn_T$) can be determined from the

potentiometric titration used to determine V_2, i.e.

$$MnO_4^- + 8H^+ + 4Mn^{2+} + 15H_2P_2O_7^{2-} \rightarrow 5Mn(H_2P_2O_7)_3^{3-} + 4H_2O \quad (6)$$

Of course, takes into consideration the Mn^{2+} added as a result of the titration to determine V_1. The fraction and absolute amount of Mn(IV) and Mn(III) species can then be determined quantitatively from the relative amounts described above in Section 2.2.1.

2.3. Structural and morphological characterization

The phase composition of the manganese dioxide samples was determined by means of a Philips PW 1710 diffractrometer, with a Cu anode that generated Cu Kα radiation (λ = 1.5418 Å). Each diffraction pattern was recorded in the 2θ range 10–80°, with a step size of 0.05° 2θ and a count time of 2.5 s per step.

The morphology of each sample was examined with a Philips XL30 scanning electron microscope at various magnifications.

2.4. Electrochemical characterization

Linear sweep voltammetry (LSV) on the resultant samples was performed using a Perkin Elmer Instruments VMP multichannel potentiostat controlled by EC-Lab software V6.80 (Princeton Applied Research). A schematic of the electrochemical cell is shown in Fig. 3. It consists of a pressed pellet of manganese dioxide and graphite (SFG6; Timrex) in a 1:10 weight ratio. The electrolyte was 37% KOH. A stainless-steel counter electrode and a Hg/HgO reference electrode complete the cell. Voltammetric scan rates of 0.05 and 0.02 mV s^{-1} were used.

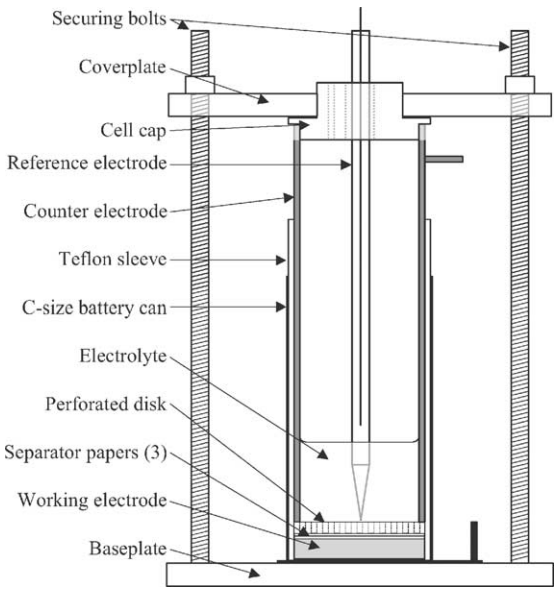

Fig. 3. Schematic of cell used for electrochemical studies.

3. Results and discussion

3.1. Synthesis

The digestion of Mn_2O_3 in H_2SO_4 solutions is believed to occur via a dissolution–precipitation mechanism that involves disproportionation of an intermediate Mn(III) species, i.e.

$$\text{dissolution}: Mn_2O_3 + 6H^+ \leftrightarrow 2Mn^{3+} + 3H_2O \quad (7a)$$

disproportionation–precipitation :

$$2Mn^{3+} + 2H_2O \leftrightarrow MnO_2 + Mn^{2+} + 4H^+ \quad (7b)$$

$$\text{overall}: Mn_2O_3 + 2H^+ \leftrightarrow MnO_2 + Mn^{2+} + H_2O \quad (7c)$$

Each of the two steps can be considered independently, and thermochemical data used to determine their respective equilibrium constants.

The dissolution step in the mechanism has been proposed on the basis of the domain of soluble Mn(III) stability in low pH solutions in the Eh-pH diagram for the Mn-H_2O system [25]. In other words, immersing Mn_2O_3 in an acidic solution is likely to result in the formation of a soluble Mn(III) intermediate, and the more concentrated the acidic solution, the greater is the concentration of Mn(III) in solution. This is reflected in the equilibrium constant for this step in the mechanism, i.e.

$$K_1 = \frac{(a_{Mn^{3+}})^2}{(a_{H^+})^6} = 6.0 \times 10^{-3}\,M^{-4} (\text{at } 25\,^\circ C) \quad (8)$$

which indicates that this reactants-favoured equilibrium requires a relatively high acid concentration to achieve significant solubilization of Mn(III).

The disproportionation–precipitation step in the mechanism has been examined previously by Welsh [26] as part of an early study into the deposition mechanism of electrolytic manganese dioxide. The author prepared suspensions of manganese dioxide in acidified Mn(II) solutions, and then examined the level of Mn(III) present in the solution after varying times. He found that the equilibrium constant was heavily products-favoured ($1.8 \times 10^6\,M^3$ at 15 °C), and increased by about an order of magnitude ($2.0 \times 10^7\,M^3$) when the temperature was increased to 100 °C. These equilibrium constants were, however, considerably less than that calculated from thermochemical data [27], i.e.

$$K_2 = \frac{(a_{Mn^{2+}})(a_{H^+})^4}{(a_{Mn^{3+}})^2} = 3.0 \times 10^9\,M^3 (\text{at } 25\,^\circ C) \quad (9)$$

As mentioned by Welsh, the equilibrium constants were based on concentrations rather than activities, which could very well explain the differences.

The equilibrium constants from thermochemical data can be combined to determine an overall equilibrium constant, which is $1.8 \times 10^7\,M^{-1}$ at 25 °C. What is most important is

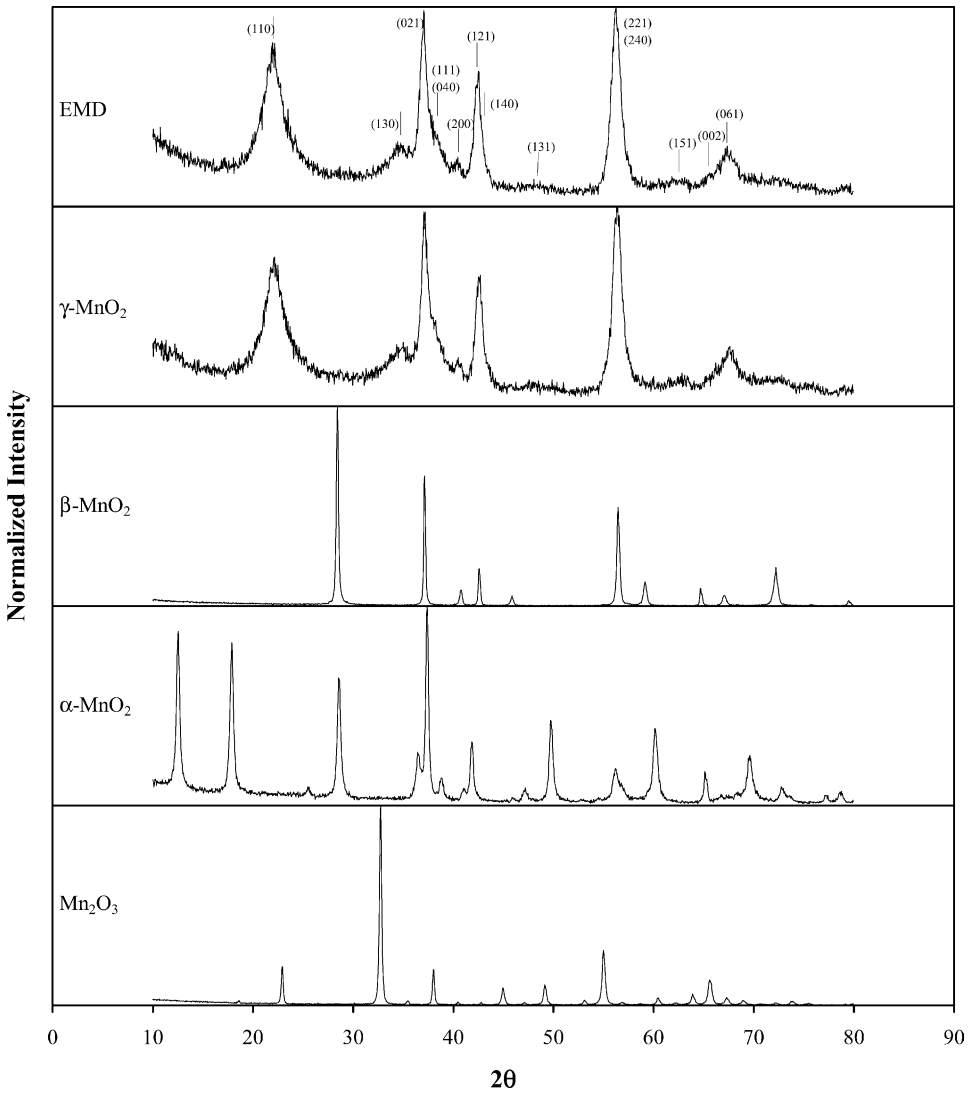

Fig. 4. Representative XRD patterns of materials prepared in this work [14].

that this value indicates that the overall reaction is heavily products-favoured. This is reflected in the yields for our digestion experiments, which approached the theoretical 55.0% of the initial Mn_2O_3 mass in all instances where reaction occurred.

3.2. Structural characterization

3.2.1. Qualitative phase identification

X-ray diffraction (XRD) was the key structural tool used in this work. An XRD pattern of the starting material (Mn_2O_3) is shown in Fig. 4, together with sample patterns of the manganese dioxide phases formed in this work. The XRD patterns for Mn_2O_3, α- and β-MnO_2 are representative of pure phases [28–30]. Furthermore, the pattern shown for γ-MnO_2 is similar to that of a typical commercial EMD, also shown in Fig. 4, although variations within this structural classification are common [5]. With the wide ranges of temperature and H_2SO_4 concentrations used here, it is also not surprising that phase mixtures have been prepared. In which case, the phase composition has been evaluated qualitatively using XRD patterns for the pure phases.

3.2.2. Phase diagram

A phase diagram for manganese dioxide is shown in Fig. 5 as a function of temperature and H_2SO_4 concentration. It is clear that there are regions of distinctly phase-pure materials, as well as less well-defined regions in which multiple phases are present, particularly at higher temperatures and H_2SO_4 concentrations. The region of experimental space leading to γ-MnO_2 is of most interest from the viewpoint of battery materials.

At low H_2SO_4 concentrations (<0.07 M), after a week of digestion at all temperatures, no reaction between Mn_2O_3 and acid was apparent. From the equilibrium described by Eq. (8), this would imply that the level of soluble Mn(III) formed in the dissolution step is relatively low, which thus inhibits the subsequent formation of manganese dioxide. This

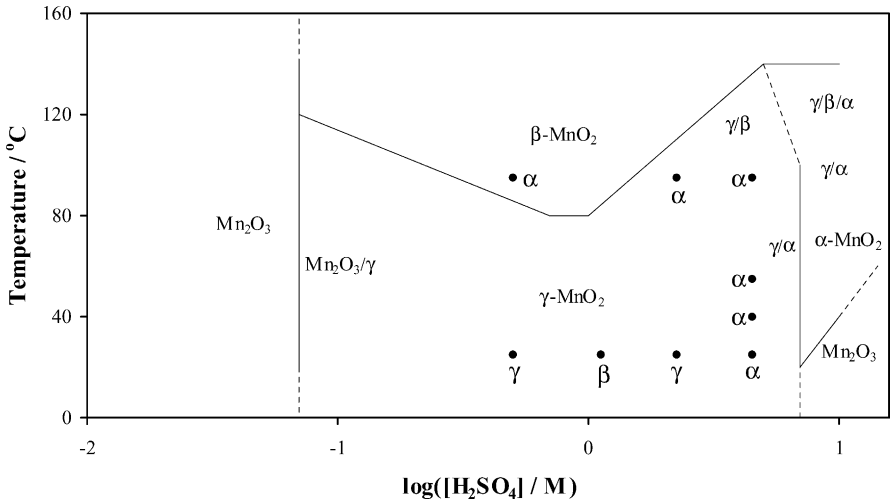

Fig. 5. Phase diagram resulting from the acid digestion of Mn_2O_3; indicates the phases found by Roussow et al. [21].

is also apparent at the Mn_2O_3–MnO_2 phase boundary where it is necessary to carry out digestion experiments with a much lower initial solids loading. Under these circumstances, the H^+:Mn_2O_3 ratio has been increased to facilitate the reaction.

Below 80 °C and as the H_2SO_4 concentration is increased, Mn_2O_3 digestion leads to the formation of γ-MnO_2. This is the preferred phase from about 0.07 M up to 5.0 M H_2SO_4. At higher H_2SO_4 concentrations, α-MnO_2 becomes the preferred phase. On the other hand, for all H_2SO_4 concentrations where manganese dioxide is formed, as the temperature is increased β-MnO_2 becomes the preferred phase. This has been observed previously by others working on understanding manganese dioxide phase transitions during EMD production [31–33]. More specifically, it has been found that if the current is interrupted during electrodeposition, then at the temperature (∼95 °C) and electrolyte composition of production (∼1 M Mn(II) and ∼0.3 M H_2SO_4), EMD undergoes a relatively rapid transition to β-MnO_2 via disproportionation (Eq. (7b)). Ultimately, the formation of β-MnO_2 is expected given that it is the most thermodynamically stable phase of manganese dioxide.

A key feature of the γ-MnO_2 stability domain is that the temperature at which the transition to β-MnO_2 occurs is elevated to ∼120 °C at both low (0.07 M) and high (5.0 M) H_2SO_4 concentrations (Fig. 5). A possible explanation for this arises from a comparison of the reaction rate between Mn_2O_3 → γ-MnO_2 and γ-MnO_2 → β-MnO_2. With β-MnO_2 being the thermodynamically stable phase, any other manganese dioxide structure included in the phase diagram is only kinetically stable over the time-frame of the digestion experiment. Therefore, the suggestion is that γ-MnO_2 is the initial phase formed as a result of the digestion and then, with time, it transforms structurally into β-MnO_2, perhaps via Eq. (7b). Therefore, the phase diagram is perhaps best interpreted in terms of the rate at which all other manganese dioxide phases convert to β-MnO_2. Below 80 °C, the activation energy is presumably too large to allow for rapid structural conversion and thus maintains the kinetic stability of γ-MnO_2. As the temperature is increased, however, there is perhaps sufficient thermal energy to overcome this activation barrier, and so the relative conversion rates become dependent on the environment within the electrolyte. At low H_2SO_4 concentrations, the amount of soluble Mn(III) present would be relatively low, i.e., the pathway to β-MnO_2 is restricted and slows down the conversion kinetics. At higher H_2SO_4 concentrations, the converse situation exists, i.e., soluble Mn(III) stability has been increased and again the formation of β-MnO_2 is inhibited. It is in this region that multiple manganese dioxide phases are observed, which can also slow down the overall conversion kinetics because different manganese dioxide phases can convert at different rates. At intermediate H_2SO_4 concentrations, the rate of soluble Mn(III) formation and its stability is such that the conversion to β-MnO_2 is optimized.

Another interesting feature of the phase diagram is the presence of apparently unreacted Mn_2O_3 at the lowest temperature and highest H_2SO_4 concentration. Under these conditions, the soluble Mn(III) species formed have their highest stability and solubility in the electrolyte. Therefore, rather than undergoing dissolution and disproportionation, the soluble Mn(III) species contribute to establishing the dissolution equilibria rather than continuing to form manganese dioxide. Furthermore, these conditions could indicate a change in the rate-determining step for the overall process due to the increased stability of the Mn(III) intermediate.

The synthesis of manganese dioxide by digestion of lower valent manganese oxides is a technique that has been used by a number of research groups for a variety of applications. One is the preparation of activated manganese dioxide for aqueous battery applications. This typically involves roasting a manganese-containing ore at high temperatures (converting it to either Mn_2O_3 or Mn_3O_4), followed by digestion in acid to form a more electrochemically active manganese dioxide, as well as to assist in the removal of some impurities. In one such example of this application [22], the roasted product

was digested in H_2SO_4 solutions that ranged in concentration from 0.6 to 6.1 M at a temperature of 90 °C for 1 h. The predominant structural form produced was α-MnO_2, in contrast with the structural data collected in this work which would suggest that the expected phase was β-MnO_2, except at high acid concentrations. The most likely explanation for this difference is the presence of impurities that originate from the ore. Metal ions such as K^+ and Ba^{2+}, which would have no doubt been in the starting ore, have a tendency to template the formation of α-MnO_2, which in itself is also a thermally stable material.

Another possible application of this synthetic procedure is the production of manganese dioxide, specifically α-MnO_2, for non-aqueous batteries. Rossouw et al. [21] started with spectroscopically-pure Mn_2O_3 and digested it under a variety of conditions that included acid type (H_2SO_4, HCl, HNO_3, CH_3COOH, H_3PO_4), concentration (0.5–9.0 M), temperature (25–95 °C) and time (1–168 h), with the goal of identifying conditions that lead to α-MnO_2 formation. Most success was had with the use of H_2SO_4, while the other acids led to either undesired phases, complete dissolution of the Mn_2O_3 or no reaction at all. The phases that were found by Rousouw et al. [21] are also shown in Fig. 5. There is consistency between the two data sets, particularly at the transition from γ- to α-MnO_2 at high acid concentrations, and the formation of γ-MnO_2 in general. There are some discrepancies, however, in particular β-MnO_2 formation at low temperatures and α-MnO_2 formation at high temperatures. These observations may be due to different digestion times. Despite the similarities, the work we have presented here represents a much more complete picture of the phases that can be produced.

3.2.3. γ-MnO_2 structural characterization

The manganese dioxide phase of most interest in this work is γ-MnO_2 due to its widespread use in alkaline Zn–MnO_2 cells. The most recent quantitative structural model for describing the XRD pattern of γ-MnO_2 has been proposed by Chabre and Pannetier [5]. Their model, which accounted for previously unexplained features of the γ-MnO_2 XRD pattern, is based first on a structural composition that consists of a microscopic intergrowth between ramsdellite and pyrolusite, as proposed originally by De Wolff [3], and hence given the name De Wolff defects (P_r). The second component of the model is based on the apparent structural similarities that pyrolusite and ramsdellite have with rutile (TiO_2) and cassiterite (SnO_2), respectively, for which twinning frequently occurs in the 0 1 1 and 0 3 1 planes. The model was therefore developed assuming twinning in the analogous 0 2 1 and 0 6 1 planes of ramsdellite (T_w). The cation vacancy model proposed by Ruetschi [4] can also be used to examine structural disorder within γ-MnO_2 samples. As described above this model accounts for structural variety through the presence of lower valent Mn(III) ions and cation vacancies in the γ-MnO_2 structure, with charge differences compensated by the presence of protons (structural water).

3.2.3.1. *De Wolff defects (P_r).*

The value of P_r can essentially be calculated from the exact position of the orthorhombic 110 peak (∼22°2θ) in the γ-MnO_2 XRD pattern, after taking into consideration the influence of microtwinning on the structure [5]. The value of P_r can loosely be interpreted in terms of the extent to which the γ-MnO_2 sample diverges from thermodynamic stability, since a P_r value of 1 indicates pure pyrolusite, which is thermodynamically stable manganese dioxide. Thermodynamic stability is mainly dependent on the core structural composition, but other features, such as cation vacancies, structural water and Mn^{3+} content also play a part. The combined effects of temperature and H_2SO_4 concentration on P_r for the γ-MnO_2 samples produced in this work are summarized in Fig. 6(a). The trends in this data are clear, namely, a decrease in H_2SO_4 concentration combined with an increase in temperature leads to a larger P_r fraction, and hence greater thermodynamic stability.

3.2.3.2. *Microtwinning (T_w).*

The proportion of microtwinning in a γ-MnO_2 sample reflects the level of defect inclusion during crystallite growth, and it can be used as an indicator of deposition conditions rate electrolyte conditions. As an example, T_w has been demonstrated to increase for samples of EMD that are deposited using high current densities [34]. Under these conditions, deposition occurs more rapidly, such that the likelihood of ordered deposition becomes less and thereby leaves the resultant γ-MnO_2 with an increasing proportion of defects. The level of microtwinning can again be calculated from the XRD pattern for γ-MnO_2, i.e., from the splitting of either the 121/140 (∼42°2θ) or 221/240 (∼56°2θ) peaks [5]. Estimating T_w in this way is open to errors because most γ-MnO_2 samples tend to have a T_w value greater than 80%, which in terms of the XRD pattern means that there is little peak separation. Consequently, the calculation is very dependent on the ability to distinguish these two peaks and so conclusions based on T_w should be treated with caution, and at best should be used as a starting point for additional research. For the γ-MnO_2 samples produced here, Fig. 6(b) shows the combined effects of temperature and H_2SO_4 concentration on the level of microtwinning. As mentioned, trends in this data are certainly less statistically significant than for P_r; but there is a small overall increase in T_w as the temperature increases and the H_2SO_4 concentration decreases.

3.2.3.3. *Mn(III) fraction (y).*

As described in Section 2, the fraction of Mn(III) ions in the γ-MnO_2 structure (y) can be quite readily determined by potentiometric titration. Its value can be interpreted as a competition between: (i) the rate of γ-MnO_2 deposition; (ii) the oxidizing power of the solution from which the γ-MnO_2 was deposited; (iii) the inherent stability of the Mn(III) ions in the electrolyte media. Points (i) and (ii) can be best understood by analogy with the production of EMD [2]. Under high anodic current densities, EMD deposition is relatively fast, which means that the product will contain a larger proportion of defects (Mn(III) ions included).

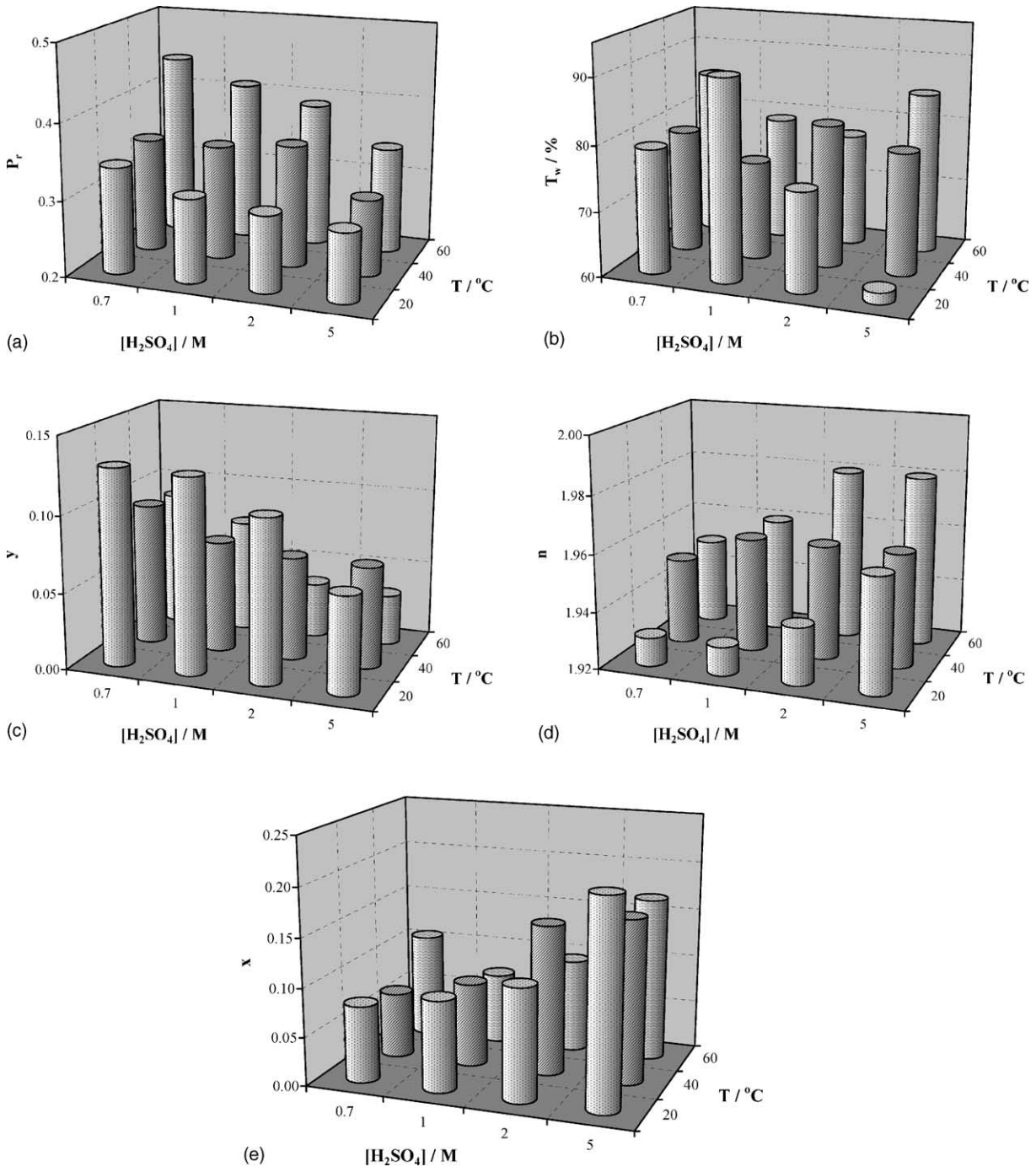

Fig. 6. Effects of temperature and H_2SO_4 concentration on (a) P_r, (b) T_w, (c) Mn(III) fraction (y), (d) n in MnO_n, (e) cation vacancy fraction (x) for γ-MnO_2 samples produced in this study.

The use of higher current densities also implies, however, that deposition is occurring at a higher voltage, or at more oxidizing conditions which infers the presence of less Mn(III). Similarly, the use of a high acid concentration will increase the EMD deposition voltage, but at the same time contribute to stabilizing Mn(III) ions both in solution and in the structure through the presence of excessive protons for charge compensation. To evaluate the competition between these processes for the samples produced in this work, Fig. 6(c) shows how the Mn(III) fraction varies with synthesis conditions. It is seen that there is a trend towards a higher y value at lower temperatures and lower H_2SO_4 concentrations. By analogy with EMD production, a higher H_2SO_4 concentration increases the solution oxidizing power from which the manganese dioxide is deposited. Therefore, the results in Fig. 6(c) suggest that this is the dominant factor in determining the γ-MnO_2 structure, despite the increased Mn(III) stability in solution under the same conditions. The role that temperature plays in

determining the Mn(III) fraction is possibly via the relative rates of the two steps in the digestion process. The inclusion of fewer Mn(III) ions into the structure at higher temperatures indicates that the disproportionation step in the mechanism, leading to MnO_2, is more efficient. This is also reflected in the n values for the MnO_n data shown in Fig. 6(d). Of course the kinetic aspects of γ-MnO_2 deposition will have to considered to determine its role in structure formation.

3.2.3.4. Cation vacancy fraction (x). The Ruetschi cation vacancy fraction is also an indicator of the level of structural defects within γ-MnO_2. It can be readily calculated from the structural water ($\%H_2O_{St}$) and total manganese content ($\%Mn_T$) of the sample using

$$x = 1 - \frac{2}{n+z} \tag{10}$$

where n is the value in MnO_n and

$$z = \frac{54.94 \times (\%H_2O_{St})}{18.016 \times (\%Mn_T)} \tag{11}$$

The results presented in Fig. 6(e) show that the cation vacancy fraction decreases as the H_2SO_4 concentration decreases and the temperature increases. Similar arguments to those used in the discussion of the Mn(III) fraction can be applied to the cation vacancy fraction because they are both indicators of structural defects. The effects of temperature on cation vacancy fraction are similar to those observed for the Mn(III) fraction. The point being that as the temperature is increased, the resultant γ-MnO_2 has a higher P_r value, which implies that it is approaching a more thermodynamically stable, less defective material. For changes in H_2SO_4 concentration, however, a different effect is observed for the cation vacancy fraction. This suggests a different controlling feature within the mechanism. With more cation vacancies apparent at higher acid concentrations, the implication is that the rate of deposition is faster under these conditions. This is despite the fact that under these conditions soluble Mn(III) ions are more stable, which would infer a longer lifetime in this state (slower reaction). Confirmation of this mechanism will come with kinetic studies. These will be the subject of a future publication.

3.2.3.5. Origins of structural variety. The approach we have taken to explain γ-MnO_2 structural variations is based on the individual components, i.e., pyrolusite and ramsdellite, and how each of the individual octahedra forming these domains are connected. Looking closely at the schematic of pyrolusite in Fig. 1, it can be seen that there are two types of [MnO_6] linkages, namely, an equatorial-equatorial edge-sharing linkage and an equatorial–axial corner-sharing linkage. Similarly, ramsdellite possesses the same types of linkage, as well as an equatorial–axial edge-sharing linkage. What is therefore needed is an understanding of the experimental conditions, such as temperature, acid content, etc., that give rise to the equatorial–axial edge-sharing linkage, since this is unique to ramsdellite.

The manganese dioxide structure formed as a result of digestion will be based on the arrangement or condensation of the soluble Mn(III) intermediate formed in solution. Soluble Mn(III) species present in an acidic aqueous electrolytes are likely to exist as hydrated complexes such as $[Mn(OH_2)_6]^{3+}$. Hydroxylation of this species, by varying the pH, occurs according to [35]

$$[Mn(OH_2)_6]^{3+} \leftrightarrow [Mn(OH_2)_5(OH)]^{2+} + H^+ \tag{12}$$

Since Mn(III) is a Jahn-Teller distorted ion in an octahedral field, axial Mn–O bonds are expected to be longer than the corresponding equatorial bonds. Therefore, the proton lost via Eq. (12) is highly likely to come from an equatorial location because there is a higher electron density between the Mn and O (shorter bond), and hence less between O and H. Condensation, as shown in Fig. 7, can then occur via the following [35]:

(i) Olation, to form an equatorial–axial corner sharing linkage (Fig. 7(a)). In this case an axial water ligand on the target for nucleophilic attack will most likely be lost due to the fact that the already longer Mn–O bond makes it a better leaving group. This leads to a single corner-sharing hydroxo-bridged linkage between octahedra that is common to both pyrolusite and ramsdellite, and so must occur irrespective of the experimental conditions.

(ii) Oxolation, to form an edge-sharing linkage (Fig. 7(b)). Here there is a concerted, or else fast sequential, linkage process in which there are two possibilities. Either an equatorial–axial linkage can occur, as in Fig. 7(b(i)), or a equatorial–equatorial linkage, as in Fig. 7(b(ii)). Based on the argument used previously, the equatorial–axial edge-sharing linkage would be preferred because it takes advantage of the axial H_2O molecule being a better leaving group. This type of edge-sharing linkage is observed only in ramsdellite. The equatorial–equatorial edge-sharing arrangement, which uses equatorial H_2O molecules as leaving groups, is present in both pyrolusite and ramsdellite, and therefore its formation must again occur irrespective of the experimental conditions.

Considering these condensation processes, the structure of γ-MnO_2 will be dependent on the amount of equatorial–axial corner-sharing (olation) relative to equatorial–axial edge-sharing (oxolation). If olation predominates, then the γ-MnO_2 will have a high P_r value. On the other hand, if the experimental conditions are such that oxolation can occur, then the resultant γ-MnO_2 will have a relatively low P_r value. With P_r increasing with temperature, it can be concluded that the formation of corner-sharing linkages predominates during condensation. This may be the result of an exothermic hydrolysis reaction (Eq. (12)), which would shift the equilibrium to the reactants side and hence form fewer hydrolyzed Mn(III) molecules. This would result in a lower likelihood of two hydrolyzed Mn(III) molecules colliding and reacting in a concerted fashion. A higher digestion temperature may

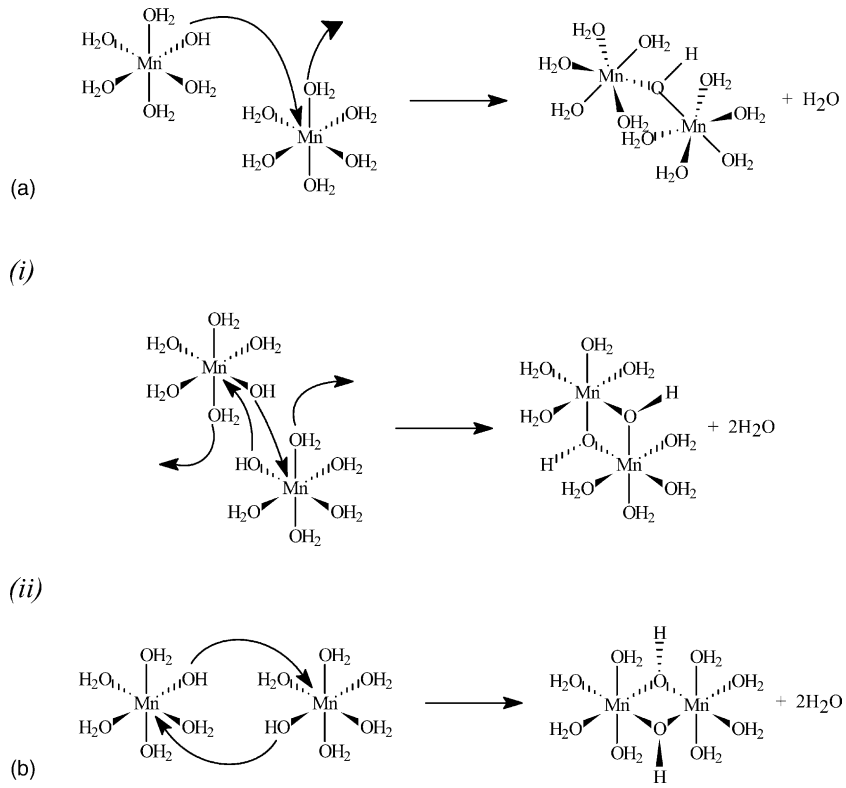

Fig. 7. Condensation of soluble Mn(III) species: (a) olation to form equatorial–axial corner-sharing linkage; (b) oxolation to form (i) equatorial–axial and (ii) equatorial–equatorial edge-sharing linkages.

also provide enough thermal energy to overcome more effectively the activation barrier for olation to occur. Whilst olation must occur to form the γ-MnO_2 structure, a higher temperature may further promote its occurrence.

The concentration of H_2SO_4 can influence the digestion process in two ways. First, increasing the H_2SO_4 concentration leads to a more soluble Mn(III) intermediate, and thus provides more of the $[Mn(OH_2)_6]^{3+}$ species for subsequent hydrolysis (Eq. (7a)). Increasing the H_2SO_4 concentration would, however, also inhibit the hydrolysis reaction (Eq. (12)), and hence limit condensation by oxolation due to the lack of hydrolyzed Mn(III) species. Clearly, a competition exists between these processes, in which fewer $[Mn(OH_2)_5(OH)]^{2+}$ molecules favours olation, and hence a higher P_r value. The experimental results show that the P_r content decreases as the H_2SO_4 concentration increases. This suggests that the dissolution reaction (Eq. (7a)) to produce more soluble Mn(III) is the dominant reaction, rather than hydrolysis suppression. Therefore, more $[Mn(OH_2)_5(OH)]^{2+}$ molecules are formed and increases the likelihood that equatorial–axial edge-sharing linkages will be formed.

As discussed above, there are many defects within the γ-MnO_2 structure and each is dependent in some way on the conditions used to prepare that sample. Given the work of Poinsignon [34], these defects (in particular microtwinning and cation vacancy fraction) can be used as a measure of crystallite growth rate, with a higher defect level produced when crystallite precipitation is quicker. With such a suggestion arising from this work, further investigation of the kinetics of dissolution and precipitation is necessary for confirmation.

3.3. Morphological characterization

Representative SEM images of both starting materials and manganese dioxide products are presented in Fig. 8. Images of commercial EMD before and after heat treatment at 550 °C to form Mn_2O_3 are shown in Fig. 8(a) and (b), respectively. The morphology of EMD consists of irregular shaped particles that have a broad particle-size distribution. These characteristics are mostly retained after heat treatment, although one significant difference of the Mn_2O_3 is that the finer particles are much more regular, with rounder edges. This is the result of inter-particle solid-state rearrangement at elevated temperatures effectively sintering the finer particles together.

After acid digestion, the macroscopic size and shape of the Mn_2O_3 particles is generally retained. By contrast, the finer surface features, typified by the various manganese dioxide structures that are formed, are found to change markedly. A typical image of γ-MnO_2 is presented in Fig. 8(c). Its morphology consists of very fine, randomly-oriented needles that are ∼250 nm long and ∼50 nm wide. These dimensions are comparable with the grain size reported by Heuer et al. [7] in a TEM study of EMD. The morphology in Fig. 8(c) is also compatible with other studies on the wet chemical syn-

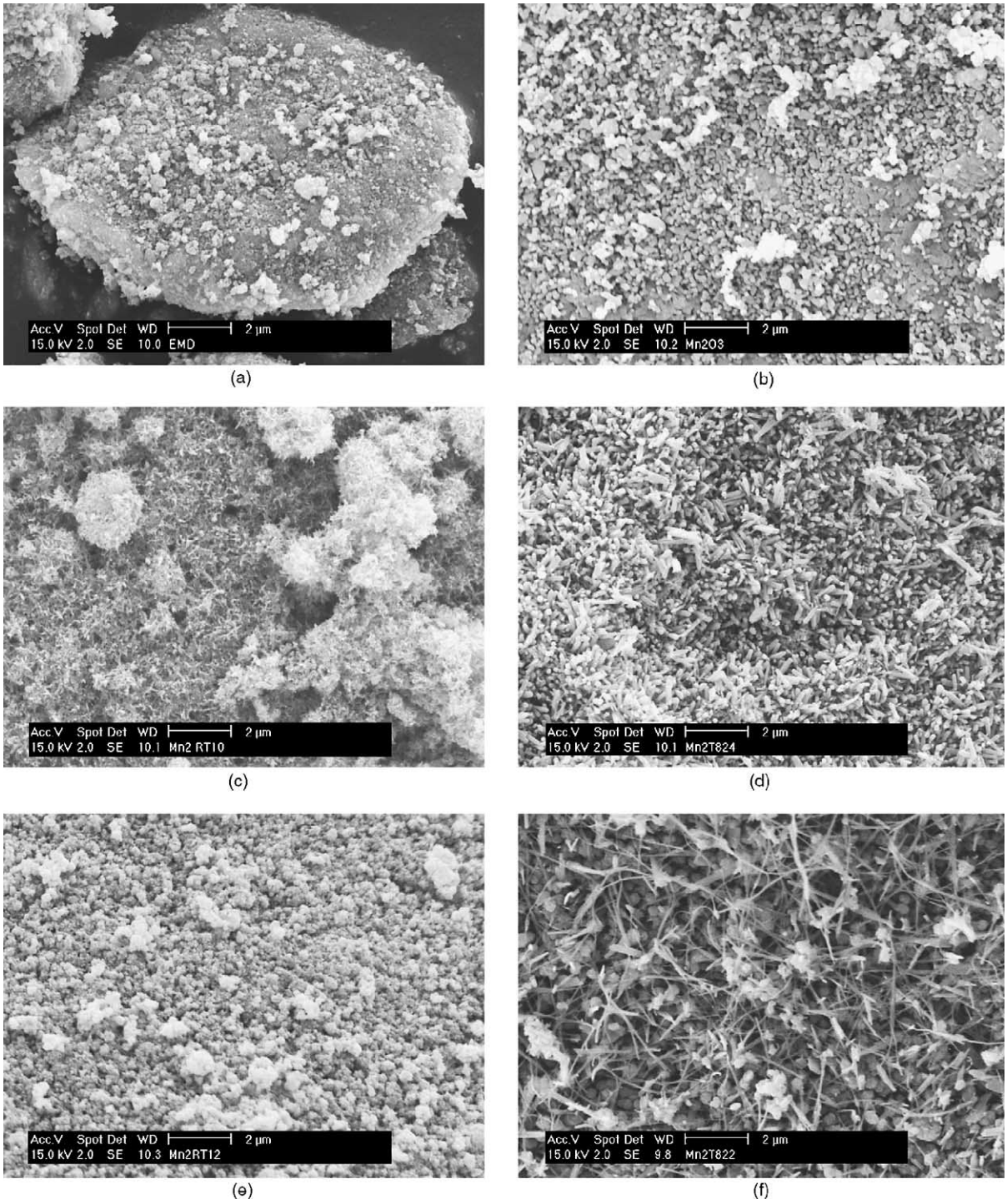

Fig. 8. SEM images of selected samples: (a) EMD; (b) Mn_2O_3; (c) γ-MnO_2; (d) β-MnO_2; (e) α-MnO_2; (f) a mixture of Mn_2O_3, β- and γ-MnO_2.

thesis of γ-MnO_2 [36]. The difference is that the grains are much more tightly packed in EMD, as compared with the relatively loose arrangement in our chemically-precipitated materials. This has consequences on the usage of these chemically precipitated materials in batteries, since the loose grain arrangement, and hence macroscopic porosity, will restrict the amount of active material that can be used in the cathode.

Within the γ-MnO_2 phase domain, slight differences in morphology are also observed due to changes in digestion conditions. Qualitatively, the size of the γ-MnO_2 needles increases with the concentration of H_2SO_4. This observation is supported by the observed trend for microtwinning and cation vacancy fraction, the levels of which also decrease as the H_2SO_4 concentration is increased. This implies that

a higher H_2SO_4 concentration leads to fewer defects within γ-MnO_2, from which larger crystallites might be expected. Clearly, this hypothesis needs to be tested further on a broader range of γ-MnO_2.

The most significant changes in morphology occur in those instances where β-MnO_2 is the digestion product (Fig. 8(d)). The surface morphology of β-MnO_2 consists of relatively large columns ∼1 μm in length and ∼100 nm wide. Furthermore, these columns appear to be somewhat more ordered, with their axes perpendicular to the particle surface. This apparent difference in crystallinity between β- and γ-MnO_2 is reflected in the XRD patterns of the materials (Fig. 4).

The surface morphology of α-MnO_2, shown in Fig. 8(e), is very similar to that of Mn_2O_3; it consists of small spherical grains up to ∼400 nm diameter. From its XRD pattern, the material is composed of crystallites of similar size to those of β-MnO_2, and so the material structure within these spherical grains must be very ordered.

When acid digestion of the Mn_2O_3 leads to a mixture of manganese dioxide phases, the resultant SEM image indicates a mixture of morphologies. As an example, Fig. 8(f) is an SEM image of a mixture of Mn_2O_3, β-MnO_2 and γ-MnO_2. Distinguishing these phases can be made by comparison with data obtained from the pure materials.

3.4. Electrochemical behaviour

3.4.1. Phase performance

The ultimate test of a battery material is its electrochemical performance. In this work electrochemical performance was evaluated using experimental conditions that focus on the intrinsic behaviour of the manganese dioxide, rather than the performance of the cathode in its entirety. Given that γ-MnO_2 is a hydrated form of manganese dioxide, with both structural and surface water, its most common application is by far in aqueous alkaline Zn–MnO_2 cells, and hence our testing regime was conducted in an appropriate electrolyte (9 M KOH). Typical voltammograms (0.05 mV s^{-1}) for each of the manganese oxide phases encountered in this work are shown in Fig. 9(a). Their corresponding capacity curves are given in Fig. 9(b). Similar behaviour is observed when a sweep rate of 0.02 mV s^{-1} is used as the discharge rate, and so only a single rate will be presented here.

The voltammograms in Fig. 9(a) clearly demonstrate the differences in electrochemical performance that result when gross changes in manganese dioxide structure are made. The voltammogram of a commercial EMD (Delta EMD, Australia Pty Limited) has been included for the purposes of comparison. Note the three component current peaks identified at +0.07, −0.12 and −0.21 V versus Hg|HgO (inset). These are believed to correspond to the solid-state reduction of Mn(IV) ions in structurally different domains within the EMD, such as around defects, and in ramsdellite and pyrolusite domains, respectively. In combination, these processes correspond to homogeneous reduction of the EMD, and represent essentially the useful capacity that can be extracted during battery usage. This reduction can be summarized by

$$(Mn^{4+})_{1-x-y}(Mn^{3+})_y(\square)_x(O^{2-})_{2-4x-y}(OH^-)_{4x+y} + \Delta H_2O + \Delta e^- \rightarrow (Mn^{4+})_{1-x-y-\Delta}(Mn^{3+})_y + \Delta(\square)_x(O^{2-})_{2-4x-y-\Delta}(OH^-)_{4x+y+\Delta} + \Delta OH^- \quad (13)$$

where Δ represents the fraction of protons and electrons inserted into the starting structure. The efficiency of this homogeneous discharge process is of course dependent on the electrode (e.g., the graphite content) and discharge rate, but in this work close to all the available capacity has been extracted. For instance, to a −0.4 V cut-off (corresponding to 1.0 V in an alkaline Zn–MnO_2 cell) Fig. 9(b) shows that ∼860 C g^{-1} has been extracted, or 77% of the theoretical capacity, assuming a dry sample and that x and y in Eq. (13) are zero. Taking into consideration typical values for the Mn^{3+} fraction ($y \approx 0.055$), however, the cation vacancy fraction ($x \approx 0.070$) and the adsorbed surface water (3–5%), account can be taken of the remaining 23% of the theoretical capacity [2].

At the completion of homogeneous discharge, ($x + \Delta$) is essentially unity. Continued discharge causes the heterogeneous reduction of what is essentially MnOOH to form $Mn(OH)_2$. This reduction process is classified as heterogeneous as it involves the formation of a solution-based Mn(III) intermediate via dissolution of the MnOOH. This is followed by Mn(III) reduction to Mn(II) in the solution phase, which subsequently precipitates as $Mn(OH)_2$. The heterogeneous process gives rise to the small asymmetric current peak at –0.44 V in the voltammogram. It is very inefficient (∼20%) due to the poor kinetics of the dissolution–precipitation mechanism, as well as the poor conductivity of both MnOOH and $Mn(OH)_2$. For EMD or γ-MnO_2 samples, the capacity associated with the process is usually associated with the surface area of the starting material, since a higher surface area would typically imply a more efficient dissolution.

The discharge of γ-MnO_2 samples produced in this work is similar to that of EMD, as shown in both Fig. 9(a) and (b). The slight differences during homogeneous discharge result from variations in the capacity associated with each of the individual reduction processes. Given that discharge is being conducted under almost ideal circumstances, these variations reflect the structural composition of the γ-MnO_2, in particular the local environment surrounding the Mn(IV) ions. What is of particular interest in the discharge of the γ-MnO_2 sample shown in Fig. 9, is the presence of more capacity at a higher voltage compared with the EMD. This is a desirable characteristic for a battery material because present trends in battery requirements are towards higher power.

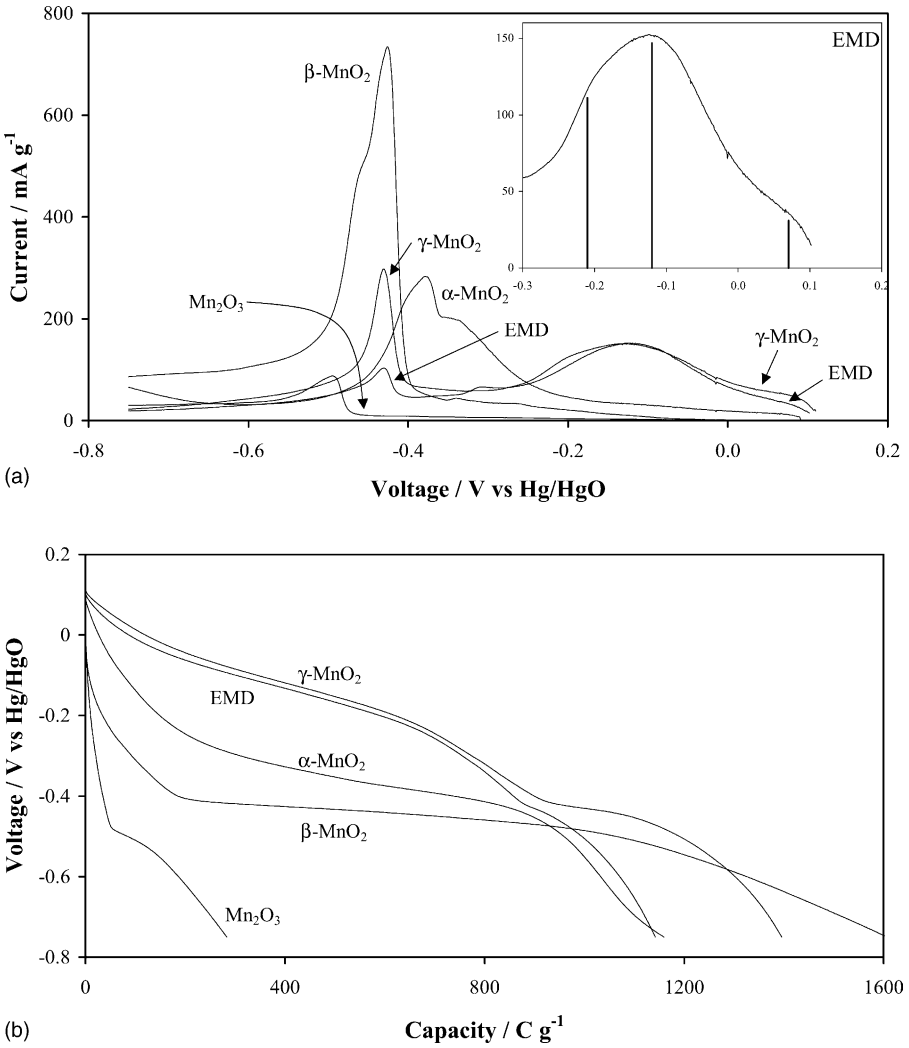

Fig. 9. Representative electrochemical discharge data for manganese oxide samples prepared in this work: (a) raw voltammetric data; (b) corresponding discharge capacity curves.

Such high voltage characteristics are absent in the discharge of all the other manganese dioxide phases. In the voltammogram for α-MnO_2, a small (∼20 mA g^{-1}), but gradually increasing current is passed from the open-circuit voltage (OCV) down to −0.2 V, after which the discharge rate accelerates. Current peaks occur at −0.35 and −0.39 V, and the bulk of the discharge capacity is extracted in these two processes. In the voltage range from the OCV down to −0.4 V, the α-MnO_2 is probably undergoing a homogeneous reduction similar to that occurring for γ-MnO_2. The differences in behaviour originate from structural differences between the phases such as the local environment around individual Mn(IV) ions, as well as the transport of reduced species (protons and electrons) through the structure. The larger 2 × 2 tunnels in α-MnO_2 [37] apparently limit its mass transport capability via the longer proton hopping distance in the structure [38], which shifts its reduction processes to lower voltages. These properties result in a lower capacity (∼740 C g^{-1}) and lower average voltage to a −0.4 V cut-off (−0.319 V).

The apparent transport limitations in the discharge of α-MnO_2 are magnified in β-MnO_2, which we believe does not undergo homogeneous reduction. The voltammogram for β-MnO_2 in Fig. 9(a) exhibits exhibited one major current peak at −0.41 V, with an attached shoulder at −0.45 V. These can be explained by considering the poor solid-state transport properties of β-MnO_2, which means that the surface becomes rapidly saturated with reduced species that cannot diffuse into the solid. As the voltage decreases, however, the surface behaves similarly to MnOOH, which undergoes dissolution and subsequent reduction to $Mn(OH)_2$. This dissolution has the added benefit of exposing a fresh manganese dioxide surface that can continue to be reduced. Overall, it should be expected, and has in fact been observed, that two linked reduction processes occur at similar voltages. For β-MnO_2, the discharge performance is dependent on the dissolution of MnOOH and the precipitation of $Mn(OH)_2$, which we have seen previously as being a relatively inefficient low-voltage process, i.e., ∼190 C g^{-1} at −0.4 V and ∼1600 C g^{-1} at −0.75 V.

For the sake of completeness, the voltammogram for Mn_2O_3 has been included in Fig. 9(a). The discharge of this material shows very little capacity above −0.48 V, below which only a small asymmetric current peak is observed. The reduction of Mn_2O_3 is very inefficient, only 283 C g^{-1} is extracted to a voltage of −0.75 V. Of course, there is no intention on our part to suggest the use of Mn_2O_3 as a battery material.

3.4.2. γ-MnO_2 discharge performance

Discharge data for the manganese dioxide phase, presented in Fig. 9 show clearly that γ-MnO_2 is the most active material electrochemically. Within the γ-MnO_2 phase domain, our interest is to identify the synthesis conditions that lead to the best-performing material. To summarize material performance we have chosen to evaluate the discharge capacity, average voltage and specific power to a −0.4 V (1.0 V in a Zn–MnO_2 cell) cut-off. Of course, to determine the specific power of manganese dioxide, the average voltage must be recalculated to indicate its voltage in an alkaline cell. Both the discharge capacity and average voltage are essentially indicators of material structure, while the specific power is an indication of the relationship between voltage and current flow, with a larger current flowing at higher voltages being preferable. These properties of the γ-MnO_2 materials are related to the conditions under which they were prepared in Fig. 10(a)–(c).

For the discharge capacity data shown in Fig. 10(a), an increase in capacity can be achieved with a decrease in both H_2SO_4 concentration and temperature over the ranges that have been considered. The samples prepared using 5 M H_2SO_4 exhibit a relatively sharp decrease in capacity, which is most probably due to the presence of some α-MnO_2 in the sample. Note that this acid concentration in the phase diagram of Fig. 5 is close to the γ- to α- transition. It is also interesting that the experimental conditions at which the capacity maximum occurs correspond to a minimum in the cation vacancy fraction (Fig. 11(a)). This is consistent with the fact that the absence of Mn(IV) ions detracts from the total available discharge capacity. Furthermore, the capacity maximum corresponds to intermediate microtwinning and De Wolff defect levels, which suggests an interaction between these two structural properties in determining performance, particularly that more defects within individual crystallites can be beneficial for performance. There is a limit to this trend, however, since if the level of De Wolff defects increases too much, the sample tends more towards β-MnO_2, which is known to behave poorly, and then overall γ-MnO_2 performance will suffer. A possible explanation for the observed behaviour is that the defects enhance the rate of mass transport (diffusion) within the solid state, perhaps by providing shorter hopping lengths for protons and electrons within the structure. An unexpected result is the increase in capacity as the Mn(III) fraction is increased (Fig. 11(b)). Clearly, any Mn(III) within the structure detracts from the total available capacity through the removal of Mn(IV) ions for discharge. It is also necessary to consider, however, that those samples with a lower Mn(III) content also have a higher P_r value. Alternatively, as the Mn(III) fraction decreases, the γ-MnO_2 becomes more thermodynamically stable (i.e., more pyrolusite) and hence less active towards discharge (cf. Fig. 9).

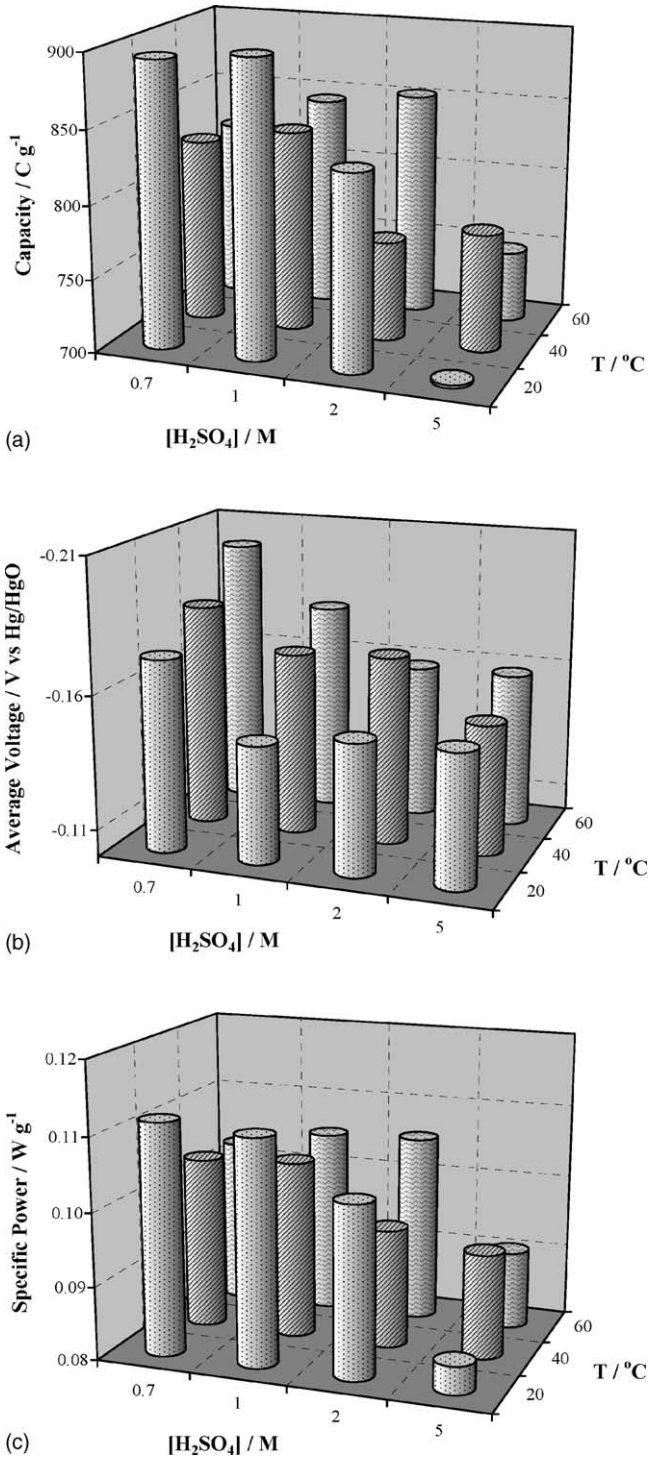

Fig. 10. Discharge characteristics of γ-MnO_2 samples prepared in this work: (a) discharge capacity to −0.4 V vs. Hg|HgO; (b) average discharge voltage; (c) specific power (assuming coupling with alkaline Zn anode).

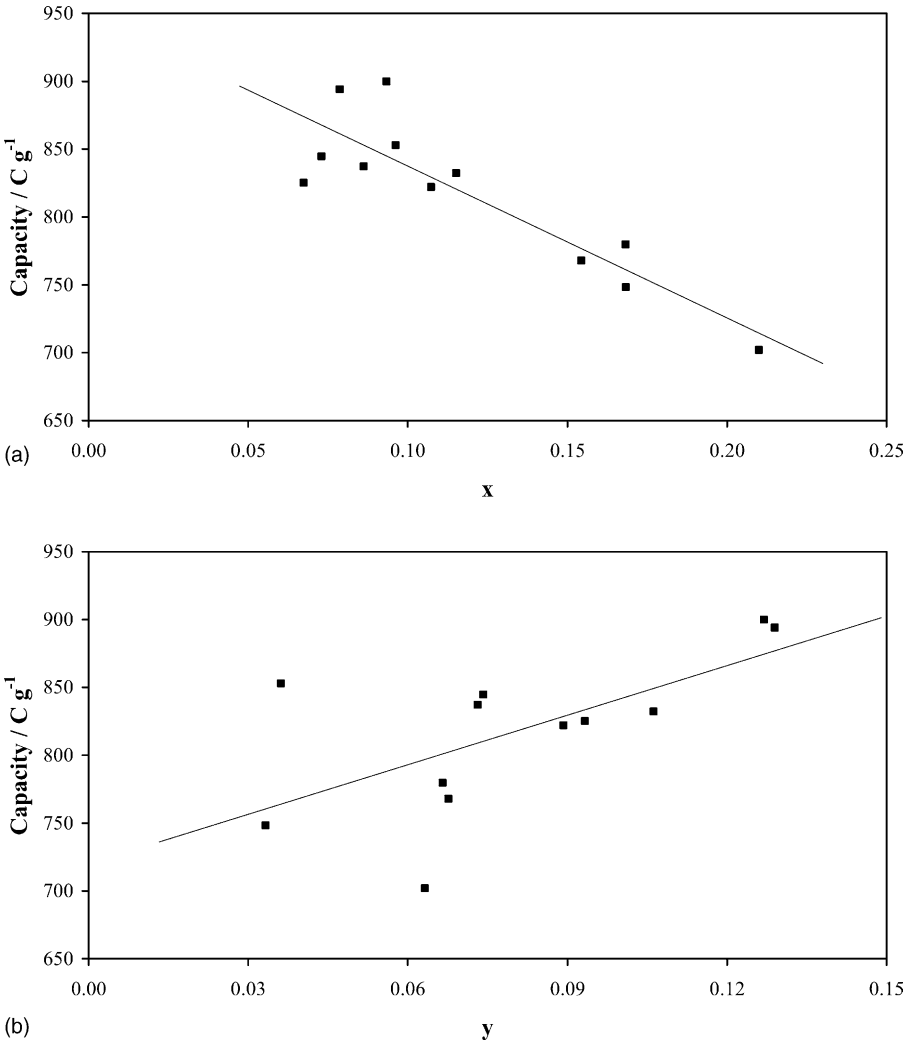

Fig. 11. Relationship between discharge capacity and (a) cation vacancy fraction (x), (b) Mn(III) fraction (y).

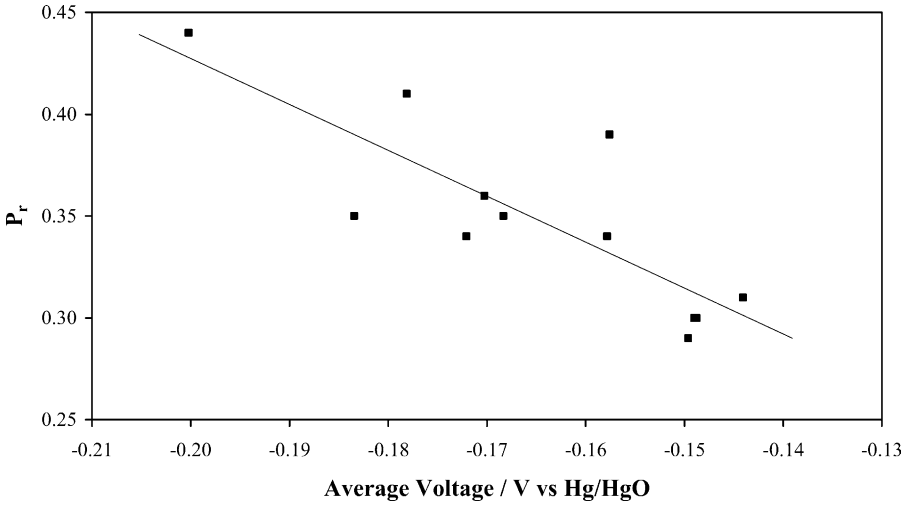

Fig. 12. Relationship between average discharge voltage and P_r for γ-MnO_2 samples prepared in this work.

While the discharge capacity is a good indicator of the preferred material structure, it discloses very little about the voltage at which the capacity is extracted. Complete material characterization requires some indication of the discharge voltage, since the trend with modern electronic devices is towards higher power demands, that, in turn, can be satisfied by higher voltage materials. In this work, the average discharge voltage is determined by calculating the voltage at which half the total discharge capacity (to −0.4 V) has been extracted. This data for the γ-MnO_2 samples produced here, suggests that the average voltage and discharge capacity are not necessarily related. The average voltage can be related to material structure, particularly P_r, as shown in Fig. 12. It is clear that as P_r decreases, the average discharge voltage increases. This result is to be expected, since Fig. 9(a) shows that the discharge of β-MnO_2 (the origin of P_r in the γ-MnO_2 structure) occurs at a much lower voltage. The relationships between the average discharge voltage and T_w, Mn(III) fraction and cation vacancy fraction are not statistically significant, which possibly suggests that their impact on the electrode voltage is minimal, although this will need to be further justified.

The specific power for these γ-MnO_2 samples is shown in Fig. 10(c). The data are essentially a combination of the discharge capacity and average voltage, and show again that the best performing materials (0.11 W g^{-1}) are produced at lower temperatures to avoid the formation of too many De Wolff defects, and at lower H_2SO_4 concentrations to introduce an appropriate T_w level.

4. Summary and conclusions

An acid digestion technique has been used to convert Mn_2O_3 into MnO_2 and soluble Mn(II) via a dissolution–precipitation disproportionation mechanism that depends on the solubility and stability of Mn(III) species in solution. The equilibrium constant for this digestion calculated from thermochemical data (1.8×10^7 M^{-1} at 25 °C), and its value reflects the complete conversion of Mn_2O_3 to the products.

Digestion experiments has been conducted in H_2SO_4 concentrations that range from 0.01 to 10.0 M, at temperatures from ambient up to 140 °C. This gives rise to a manganese dioxide phase diagram in which the γ- phase predominates, except at high H_2SO_4 concentrations (>5 M) where α-MnO_2 forms, and at high temperatures (>80 °C) where β-MnO_2 forms. The structure of the γ-MnO_2 samples is interpreted using De Wolff defects (P_r), microtwinning (T_w), cation vacancy fraction (x), and Mn(III) fraction (y). The following trends are observed:

(i) Increase P_r: increase temperature decrease H_2SO_4 concentration.
(ii) Increase y: decrease temperature decrease H_2SO_4 concentration.
(iii) Increase x: decrease temperature increase H_2SO_4 concentration.

Some trends in the T_w data are observed, but the interpretation is found to be problematic due to the wide ranging T_w values that result from the difficulty in resolving the XRD peaks that lead to the T_w values. These trends in structure are interpreted on the molecular level in terms of soluble Mn(III) intermediate condensation, in particular the competition between equatorial–axial edge-sharing to form a ramsdellite domain and equatorial–axial corner-sharing to form extended pyrolusite (β-MnO_2) domains. It is concluded that decreasing the temperature and increasing the H_2SO_4 concentration results in a greater proportion of the equatorial–axial edge-sharing linkage (ramsdellite domains) within the γ-MnO_2 structure.

In morphological terms each of the manganese dioxide phases have their own distinctive physical appearance. γ-MnO_2 is always observed to be present as fine needles, on average about 250 nm × 50 nm in size, β-MnO_2 is present as much larger columns about 1 μm × 100 nm in size, while α-MnO_2 is present as small spheres of up to 400 nm in diameter. The morphology of α-MnO_2 is very similar to the starting Mn_2O_3.

Electrochemical characterization of each of the phases shows that the best-performing samples of γ-MnO_2 have a discharge capacity that is comparable with that of commercial EMD (858 C g^{-1} to a −0.4 V cut-off) and represents an almost 100% extraction of the available capacity. These samples also exhibit the three expected component processes during homogeneous reduction. The α- and β-MnO_2 phases produced are inferior in terms of electrochemical performance due to the predominance of inefficient low-voltage discharge processes.

Within the bounds of γ-MnO_2 phase stability, it is interesting to note that superior materials are prepared at low temperature and low H_2SO_4 concentration. These conditions correspond to a minimum in the cation vacancy fraction, as is anticipated, but at intermediate P_r and T_w values. An excessive P_r value can be seen to be detrimental to performance because the sample will be approaching the limit of β-MnO_2, which is a poor performer. The observed presence of an intermediate level of defects may be beneficial to mass transport within the γ-MnO_2 structure due to a lessening of the hopping distance for protons and electrons moving through the structure.

Acknowledgements

D.W. would like to acknowledge the receipt of an ADS scholarship as part of the AusAID scheme. He would also like to thank the Universitas Tadulako, Palu, for granting a leave of absence to continue his studies in Australia. Dr. Rodney Williams from Delta EMD Australia Pty Limited is also acknowledged for both technical discussions and EMD provision.

References

[1] C.B. Ward, A.I. Walker, A.R. Taylor, Prog. Batt. Batt. Mater. 11 (1992) 40.
[2] R.P. Williams, Ph.D. thesis, University of Newcastle, 1996.
[3] P.M. De Wolff, Acta Cryst. 12 (1959) 341.
[4] P. Ruetschi, J. Electrochem. Soc. 131 (1984) 2737.
[5] Y. Chabre, J. Pannetier, Prog. Solid State Chem. 23 (1995) 1.
[6] S. Turner, P.R. Buseck, Nature 304 (1983) 143.
[7] A.H. Heuer, A.Q. He, P.J. Hughes, F.H. Feddrix, ITE Lett. Batt., New Technol. Med. 1 (2000) 926.
[8] A. Kozawa, J.F. Yeager, J. Electrochem. Soc. 112 (1965) 959.
[9] A. Kozawa, T. Kalnoki-Kis, J.F. Yeager, J. Electrochem. Soc. 113 (1966) 405.
[10] A. Kozawa, R.A. Powers, J. Electrochem. Soc. 113 (1966) 870.
[11] A. Kozawa, R.A. Powers, Electrochem. Tech. 5 (1967) 535.
[12] A. Kozawa, R.A. Powers, J. Electrochem. Soc. 115 (1968) 122.
[13] A. Kozawa, J.F. Yeager, J. Electrochem. Soc. 115 (1968) 1003.
[14] D.A.J. Swinkels, K.E. Anthony, P.M. Fredericks, P.R. Osborn, J. Electroanal. Chem. 168 (1984) 433.
[15] Z. Hong, C. Zhenhai, X. Xi, J. Electrochem. Soc. 136 (1989) 2771.
[16] S.W. Donne, G.A. Lawrance, D.A.J. Swinkels, J. Electrochem. Soc. 144 (1997) 2949.
[17] S.W. Donne, G.A. Lawrance, D.A.J. Swinkels, J. Electrochem. Soc. 144 (1997) 2954.
[18] S.W. Donne, G.A. Lawrance, D.A.J. Swinkels, J. Electrochem. Soc. 144 (1997) 2961.
[19] T. Ohzuku, H. Higashimura, T. Hirai, Electrochim. Acta 29 (1984) 779.
[20] T. Ohzuku, M. Kitagawa, K. Sawai, T. Hirai, J. Electrochem. Soc. 138 (1991) 360.
[21] M.H. Rossouw, D.C. Liles, M.M. Thackeray, Prog. Batt. Batt. Mater. 15 (1996) 8.
[22] W.S. Li, L.C. Jiang, G.Y. Xie, X. Jiang, J. Power Sources 58 (1996) 235.
[23] K.J. Vetter, N. Jaeger, Electrochim. Acta 11 (1966) 401.
[24] A.I. Vogel, Quantitative Chemical Analysis, fifth ed., Wiley, New York, 1989.
[25] M. Pourbaix, Atlas of Electrochemical Equilibria in Aqueous Solutions, Pergamon Press, London, 1966.
[26] J.Y. Welsh, Electrochem. Tech. 5 (1967) 504.
[27] D.R. Lide (Ed.), Handbook of Chemistry and Physics, 73rd ed., 1992.
[28] JCPDS File 73-1826 (Mn_2O_3).
[29] JCPDS File 72-1982 (α-MnO_2, cryptomelane).
[30] JCPDS File 01-0799 (β-MnO_2, pyrolusite).
[31] W.H. Kao, C.W. Gross, R.J. Ekern, J. Electrochem. Soc. 134 (1987) 1321.
[32] W.H. Kao, J. Electrochem. Soc. 135 (1988) 1317.
[33] W.H. Kao, J. Electrochem. Soc. 136 (1989) 13.
[34] C. Poinsignon, Mol. Cryst. Liq. Cryst. 311 (1998) 129.
[35] C.J. Brinker, G.W. Scherer, Sol–Gel Science: The Physics and Chemistry of Sol–Gel Processing, Academic Press, San Diego, 1989.
[36] E.I. Wang, L. Lin, W.L. Bowden, US Patent 5,277,890, 1994.
[37] R.G. Burns, V.M. Burns, in: A. Kozawa, R.J. Brodd (Eds.), Proceedings of the Manganese Dioxide Symposium, vol. 1, Cleveland, 1975, p. 306.
[38] D. Balachandran, D. Morgan, G. Ceder, A. van de Walle, J. Solid State Chem. 173 (2003) 2.